RSC Advances

PAPER

View Article Online
View Journal | View Issue

Check for updates

Cite this: *RSC Adv.*, 2017, **7**, 53810

Formation of intrinsic and silicon defects in MoO_3 under varied oxygen partial pressure and temperature conditions: an *ab initio* DFT investigation

D. S. Lambert,*[a] S. T. Murphy,[b] A. Lennon[a] and P. A. Burr[c]

Molybdenum trioxide (MoO_3) is a promising material for energy conversion applications, including recent uses as a hole selective contact in silicon photovoltaic devices. The electrical and chemical properties of MoO_3 are known to be strongly sensitive to the presence of intrinsic and extrinsic defects, which in turn are dependent on the fabrication route and processing conditions used to form the device layers. Of particular interest to this study were intrinsic defects comprising oxygen vacancies and extrinsic defects involving possible contaminant silicon atoms. Density functional theory simulations were used to predict defect concentrations as a function of processing temperature and oxygen partial pressure. A rigorous method is outlined to calculate defect formation energies for all intrinsic defects in MoO_3, resolving conflicting information arising from previous studies. Brouwer diagrams were constructed and used to show that the charge neutral oxygen vacancy is dominant under most of the temperature and oxygen partial pressure conditions investigated. It was also shown that at commonly-used processing temperatures and oxygen partial pressures, silicon interstitials in MoO_3 can introduce a spin-polarised defect state 0.5 eV above the MoO_3 valence band maximum. Their concentration in MoO_3 may reach 1.3 ppm with processing conditions of 700 K and 10^{-6} atm oxygen partial pressure, and this concentration is predicted to increase dramatically with higher temperatures and/or lower oxygen partial pressures. Our findings highlight the possibility of silicon contamination in hole-selective contact layers for silicon photovoltaic devices, with a potential increase in the parasitic absorption due to silicon defects in the contact layers reducing energy conversion efficiency.

Received 27th September 2017
Accepted 10th November 2017

DOI: 10.1039/c7ra10690d

rsc.li/rsc-advances

Open Access Article. Published on 23 November 2017. Downloaded on 2/3/2026 3:27:22 PM.
This article is licensed under a Creative Commons Attribution 3.0 Unported Licence.

Introduction

The worldwide search for efficient and cost-effective energy conversion and storage systems has resulted in the investigation of new uses for lesser known materials. Molybdenum trioxide and its sub-stoichiometric form (MoO_{3-x}; $0 < x < 1$) is a material with proposed applications in batteries,[1–3] electrochemical capacitors,[4–8] sensors,[9,10] catalysis,[11–13] photo-catalysis,[14,15] electrochromism and photochromism.[16–18] It has also been found to be an effective hole transport layer in semiconductor devices[19–21] and a range of photovoltaic cells.[20–22]

Sub-stoichiometric molybdenum trioxide was first reported as a contact layer for organic,[23–25] kesterite[26] and perovskite[27–30] solar cells, however recently it has also found application as a hole-selective contact for higher efficiency silicon heterojunction cells. It has a large workfunction of 5.7 eV and wide band gap of 3.3 eV, which allows an electrical contact to achieve high hole selectivity without inducing significant parasitic absorption.[22] Battaglia *et al.*[22] found that by replacing the p-type amorphous silicon hole contact layer with amorphous MoO_{3-x}, the short circuit current density could be increased by 1.9 mA cm^{-2}, although a reduction in fill factor degraded the overall efficiency. The low fill factor was subsequently addressed by Geissbühler *et al.*[31] by limiting the processing temperature for devices to 130 °C. This enabled them to achieve an energy conversion efficiency of 22.5% for silicon heterojunction cells. However, this achievement still falls short of the record efficiency of 24.7% [32] for a two-side contacted heterojunction cell, and the low processing temperature is incompatible with other manufacturing processes such as silver screen-printing. In order to overcome these problems, Cauduro *et al.*[33] recently proposed that controllable crystallisation of reactive-sputtered films of MoO_{3-x} can be used to form films with a high workfunction and a highly ordered nanocrystalline sublayer structure that may enhance carrier mobility and allow for higher processing temperatures. Sook *et al.*[34] have also

[a]School of Photovoltaics and Renewable Energy Engineering, The University of New South Wales, Sydney, NSW 2052, Australia. E-mail: d.lambert@student.unsw.edu.au
[b]Department of Engineering, Lancaster University, Bailrigg, Lancaster, LA1 4YW, UK
[c]School of Electrical Engineering and Telecommunications, The University of New South Wales, Sydney, NSW 2052, Australia

This journal is © The Royal Society of Chemistry 2017

Open Access Article. Published on 23 November 2017. Downloaded on 2/3/2026 3:27:22 PM.
This article is licensed under a Creative Commons Attribution 3.0 Unported Licence.

reported that crystalline MoO_{3-x} has improved mobility and lower resistivity than amorphous MoO_{3-x}, and has material properties that are highly dependent on preparation conditions. Consequently, in order to realise the full potential of MoO_{3-x} as a low-cost hole transport layer for silicon solar cells, it is necessary to understand how preparation conditions affect the material's structural and electrical properties, as well as it's compatibility with silicon substrates.

Sub-stoichiometric molybdenum trioxide can be prepared by a number of techniques such as thermal oxidation,[35] spray pyrolysis,[36] or reactive sputtering.[34,37] The most common preparation method involves a two-step process, where MoO_3 powder is first thermally-evaporated onto a substrate, and then the resulting film is annealed at high temperature.[38,39] The conditions of preparation affects the defect chemistry, in particular by the formation of oxygen vacancies[35] and, if enough vacancies form, then the material can amorphize.[40] The stoichiometry of MoO_{3-x} has been shown to influence many important properties of the material, such as work function,[35] battery capacity,[41] band gap,[38,42,43] conductivity,[44] and optical reflectance.[45] Point defects are also believed to create a defect band within the band gap of MoO_{3-x}, which is thought to be crucial for selective carrier extraction.[22] A mechanistic understanding of the sensitivity of defect chemistry to deposition method and post-deposition processing is needed in order to tailor the properties of MoO_{3-x} for device applications.

Crystalline α-MoO_3 has a structure consisting of layers of distorted octahedral, joined along the *b*-axis by van der Waals forces, as shown in Fig. 1. Three distinct oxygen sites exist in MoO_3, with different coordination. The O1 oxygen atom, sometimes referred to as the terminal oxygen, is connected to only one Mo atom and extends along the *b*-axis into the van der Waals planes. The O2 oxygen atom, also known as the asymmetric oxygen, has two bonds to molybdenum atoms, of different length. The O3 atom is triply coordinated and has been called the symmetric oxygen, as the in-plane bonds with molybdenum atoms are the same length. Oxygen vacancies may form at each of these sites.

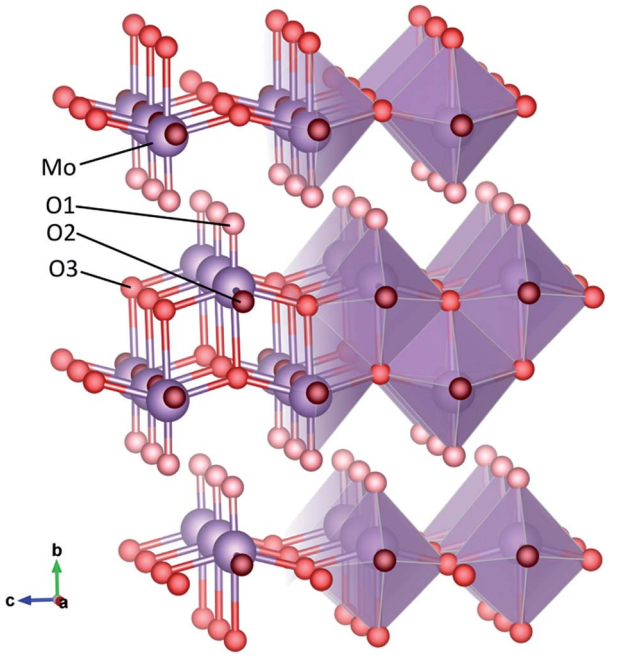

Fig. 1 Structure of crystalline MoO_3 in ball-and-stick and polyhedral representation. The molybdenum (Mo) atom is in purple and the three oxygen (O) sites are in three different shades of red.

Density functional theory (DFT) calculations have been used to determine the oxygen vacancy formation energies at each site in previous studies,[46–49] however these studies have used different methodologies and yielded results that are highly inconsistent with each other. The formation energy of molybdenum vacancies was considered in one study,[48] but the formation energy of molybdenum and oxygen interstitials is still not known. In this study, a well-defined and consistent method is used to analyse the formation energy of all intrinsic defects, and then these are related to real-life defect concentrations at various experimental conditions of temperature and oxygen partial pressure through the construction of Brouwer diagrams.

Since many of the selective contact applications involve MoO_{3-x} in contact with silicon surfaces,[20,22] silicon defects within bulk MoO_3 are also studied in this paper. A study by Anwar *et al.*[50] on Si–MoO_3 mixtures suggested that silicon atoms may penetrate MoO_3 and that these atoms could reduce the electrical conductivity. Previously, extrinsic defects in MoO_3 crystals such as Na,[47] Li[3,51] and H[52,53] have been studied with DFT, but so far DFT studies of the interaction between MoO_3 and silicon have only examined molybdenum oxides on silica surfaces.[54–56] In this paper, the possibility of silicon diffusion in crystalline MoO_3 is investigated and its effect on electronic properties is explored.

Methodology

Computational details

Density functional theory calculations were performed with the projector augmented wave approach using the Vienna ab-initio simulation package (VASP).[57] Simulations in DFT require the choice of an exchange–correlation functional among other important parameters in order to balance accuracy with computational complexity. For this study, the PBE-GGA functional[58] was used with the addition of an on-site Coulomb correction ($+U$) of 6.3 eV in order to improve the localisation of d-electrons in molybdenum using the simplified rotationally invariant formalism of Dudarev *et al.*[59] in line with previous work on MoO_3.[52,60,61] In order to account for the significant effect of van der Waals forces in this material, the semi-empirical DFT-D3 energy correction by Grimme *et al.*[62] was used. While a number of different parameters have been used in the modelling of MoO_3 in the past, as is outlined in the Model verification subsection, the parameters chosen for this paper provide accurate results without excessively long simulation times.

The Brillouin zone was sampled with a $3 \times 1 \times 2$ *k*-point mesh for the supercell of choice, $2 \times 2 \times 3$. The choice of supercell shape and size is justified in the subsection Charge

Open Access Article. Published on 23 November 2017. Downloaded on 2/3/2026 3:27:22 PM.
This article is licensed under a Creative Commons Attribution 3.0 Unported Licence.

correction. Simulations were performed with a plane wave basis set energy cut-off of 500 eV, and a Gaussian smearing of the partial occupancies was applied with a width of 0.1 eV to speed up the simulations. The density of states were obtained by performing an additional single point calculation after geometry optimisation using a denser k-point mesh of $6 \times 2 \times 4$ k-points and interpolating with the tetrahedron method with Blöchl corrections. The static ion-clamped dielectric tensor and elastic constants were calculated with density functional perturbation theory. For elastic constant calculations, both lattice and atoms were displaced in steps of ± 0.005 Å and ± 0.01 Å.

Formation energies

Defect formation energies were calculated according to eqn (1)

$$E_{\text{formation}} = E_{\text{defect}} - E_{\text{host}} + \sum_j \Delta n_j \mu_j + q(E_{\text{VBM}} + \mu_e) + E_{\text{chgcor}} \quad (1)$$

where E_{defect} and E_{host} are the DFT energies of the defective and perfect supercells, the summation term refers to the chemical potential μ of removed (positive) or added (negative) atoms, E_{VBM} is the energy of an electron at the valence band minimum, μ_e is the Fermi level relative to E_{VBM}, and E_{chgcor} is the energy correction applied for charged defects to counter the self-interaction across the periodic boundary conditions of finite supercells.

Chemical potentials

The chemical potentials used in eqn (1) have a large effect on defect formation energies, and must be determined carefully. The chemical potentials of molybdenum and oxygen atoms within the MoO_3 crystal are derived from the chemical potentials of the same atoms in reservoirs of BCC-Mo(s) crystal and O_2(g) respectively. To overcome the well-known limitation of GGA-DFT inaccurately modelling oxygen gas molecules,[63] the method of Finnis *et al.*[64] is used to derive the chemical potential of oxygen in O_2 gas, $\mu_{O_2(g)}$, from the equation for standard formation energy of MoO_3:

$$\Delta G_f^{MoO_3}\left(p_{O_2}^0, T^0\right) = \mu_{MoO_3(s)} - \mu_{Mo(s)} - \frac{3}{2}\mu_{O_2(g)}\left(p_{O_2}^0, T^0\right) \quad (2)$$

where $\Delta G_f^{MoO_3}$ is the experimental standard formation energy of MoO_3 with a value of -668.079 kJ mol^{-1},[65] and the chemical potentials $\mu_{MoO_3(s)}$ and $\mu_{Mo(s)}$ are the DFT total energies of MoO_3 and BCC-Mo respectively, normalised per formula unit. The assumption is made that the chemical potentials of the MoO_3 and BCC-Mo(s) crystals are not strongly dependent on partial pressure and temperature, but that the potential of the oxygen gas will change according to the rigid-dumbbell ideal gas law:

$$\mu_{O_2(g)}\left(p_{O_2}, T\right) = \mu_{O_2(g)}\left(p_{O_2}^0, T^0\right) + \Delta\mu(T) + \frac{1}{2}k_B T \log\left(\frac{p_{O_2}}{p_{O_2}^0}\right) \quad (3)$$

$$\Delta\mu(T) = -\frac{1}{2}\left(S_{O_2}^0 - C_p^0\right)\left(T - T^0\right) + C_p^0 T \log\frac{T}{T^0} \quad (4)$$

To test these assumptions, the expected free energy of formation at 700 K was calculated with eqn (2)–(4) to be -588 kJ mol^{-1}, close to the experimental value of -567 kJ mol^{-1}.[65]

The total chemical potential of a formula unit of MoO_3 is the sum of the chemical potentials of its component parts inside the MoO_3 crystal:

$$\mu_{MoO_3(s)} = \mu_{Mo(MoO_3)} + 3\mu_{O(MoO_3)} \quad (5)$$

At equilibrium, the chemical potentials of atoms inside the crystal cannot be larger than that of the reservoirs outside. Within these bounding cases, the assumption is made that the chemical potential of oxygen in MoO_3 is equal to that of oxygen gas, which better describes the case of O-rich condition. Thus, the chemical potentials of oxygen and molybdenum in MoO_3 are:

$$\mu_{O_2(MoO_3)}(p_{O_2}, T) = \mu_{O_2(g)}(p_{O_2}, T) \quad (6)$$

$$\mu_{Mo(MoO_3)}\left(p_{O_2}, T\right) = \mu_{MoO_3(s)} - \frac{3}{2}\mu_{O_2(g)}\left(p_{O_2}, T\right) \quad (7)$$

Where silicon impurities are considered, the chemical potential of silicon was calculated with the same procedure from DFT simulations of α-quartz SiO_2, and assuming that it was in equilibrium with oxygen gas.

Charge correction

When charge is introduced into a supercell with periodic boundary conditions, an energy shift results from both the charge interaction between the repeating cells[63] and from the background uniform charge jellium introduced to compensate for this.[66] The magnitude of the required correction is a function of the screened Madelung potential, ν_M^{scr}, calculated in an anisotropic medium with the following equation:[67]

$$\nu_M^{scr} = \sum_{\boldsymbol{R}_i}^{i\neq 0} \frac{1}{\sqrt{\det\bar{\varepsilon}}} \frac{\operatorname{erfc}\left(\gamma\sqrt{\boldsymbol{R}_i\bar{\varepsilon}^{-1}\boldsymbol{R}_i}\right)}{\sqrt{\boldsymbol{R}_i\bar{\varepsilon}^{-1}\boldsymbol{R}_i}} + \sum_{\boldsymbol{G}_i}^{i\neq 0} \frac{4\pi}{V_c} \frac{\exp\left(-\boldsymbol{G}_i\bar{\varepsilon}^{-1}\boldsymbol{G}_i/4\gamma^2\right)}{\boldsymbol{G}_i\bar{\varepsilon}^{-1}\boldsymbol{G}_i} - \frac{2\gamma}{\sqrt{\pi\det\bar{\varepsilon}}} - \frac{\pi}{V_c\gamma^2} \quad (8)$$

where γ is a convergence parameter, $\boldsymbol{R}$ and $\boldsymbol{G}$ are the real and reciprocal lattice vectors and $\bar{\varepsilon}$ is the dielectric tensor. Thus, in an anisotropic medium, the Madelung potential can be zero or negative for certain lattice vectors.[66] To demonstrate the effect of Madelung potential, the +1 charged O1 oxygen vacancy ($V_O^{\cdot}$ using Kröger–Vink notation[68]) was simulated in different supercell sizes and shapes. The resulting formation energy is shown as a function of the Madelung potential in Fig. 2. The uncorrected formation energy when using a $3 \times 1 \times 3$ supercell is 0.25 eV lower than that from a $2 \times 2 \times 3$ supercell. The amount of correction required is proportional to the square of the amount of charge introduced,[69] so for simulations involving high charges such as $V_O^{\cdot\cdot}$ or $V_{Mo}^{''''''}$ it is essential to have an accurate method of correcting for charged defects.

 This journal is © The Royal Society of Chemistry 2017

Open Access Article. Published on 23 November 2017. Downloaded on 2/3/2026 3:27:22 PM.
This article is licensed under a Creative Commons Attribution 3.0 Unported Licence.

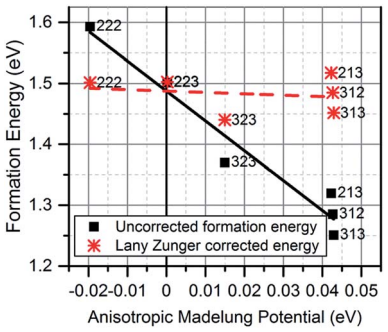

Fig. 2 Defect formation energy of $V_O^{\cdot\cdot}$ as a function of Madelung potential, before (black solid) and after (red dashed) applying the approximate Lany and Zunger charge correction.[70] The labels indicate the dimensions of the supercell used (in terms of unit cell replicas).

The $3 \times 1 \times 3$ supercell has nearly equal simulation lengths in the a, b, and c directions, and has been used by most previous studies to model point defects.[47,48] However, when considering the anisotropic character of the dielectric constant, it is apparent that the $2 \times 2 \times 3$ supercell has near-zero Madelung potential, yielding a very small Coulomb self-interaction energy. For the very highly charged defect of $V_{Mo}^{''''''}$, a first order approximation to the charge correction yields a charge correction less than 0.5 eV, and it has been shown that this is an overcorrection that should be scaled down further to correct for local screening,[70] indicating that the use of this supercell shape removes almost all of the uncertainties associated with the use of approximate charge correction schemes.

It is important to note that finite size effects may also arise from elastic self-interaction,[71,72] which are dependent on the anisotropic elastic constant tensor. Since the elastic tensor is distinctly different from the dielectric tensor, a compromise must be struck between elastic and electrostatic self-interaction when choosing the optimal supercell shape. Nevertheless, the moderate permittivity and comparatively large stiffness of MoO_3, shown in Tables 1 and 2, means that the magnitude of the charge self-interaction energy is considerably larger than that of elastic self-interaction. Therefore, the current work was carried out using the $2 \times 2 \times 3$ supercell.

The V_{O2} defects, which were stable in the $3 \times 1 \times 3$ supercell, were not stable in this supercell, collapsing onto the O1 site. Akande *et al.*[48] report nearly identical formation energies for vacancies on the O2 and O1 sites, suggesting that this collapse was not a unique feature of our methodology. Nevertheless, the V_{O2} defect formation energy was calculated in a larger supercells

Table 1 Static dielectric tensor for MoO_3 calculated along the $\varepsilon_{11}^{\infty}$, $\varepsilon_{22}^{\infty}$ and $\varepsilon_{33}^{\infty}$ directions corresponding to the direct lattice vectors a, b and c, along with average dielectric value, compared to previous work, both DFT from Lajaunie *et al.*[73] and experimental from Deb & Chapoorian[40]

Direction	$\varepsilon_{11}^{\infty}$	$\varepsilon_{22}^{\infty}$	$\varepsilon_{33}^{\infty}$	Average
This work	5.8	4.2	6.1	5.4
Previous DFT	5.5	4.2	6.3	5.3
Experimental	—	—	—	5.7

Table 2 Calculated elastic constants (c_{ij}), bulk modulus (K), shear modulus (G) and Young modulus (E) of MoO_3, in GPa. In brackets, experimental values from Du *et al.*[74] K and G were obtained with the Reuss–Voigt–Hill average method,[75] and E was obtained through homogeneous (isotropic) linear elastic theory

c_{11}	c_{22}	c_{33}	c_{12}	c_{13}	c_{23}	c_{44}	c_{55}	c_{66}	K	G	E
263	96	340	41	72	51	98	64	57	98	74	176 (65)

($4 \times 4 \times 6$, $3 \times 1 \times 3$, $2 \times 2 \times 2$, $3 \times 2 \times 2$), and it was consistently found to either collapse into V_{O1} or be much less favourable than V_{O1} for all charge states and in all supercell sizes investigated, thus the omission of these defects does not have a significant effect on the predicted defect concentrations.

Brouwer diagram

Brouwer diagrams provide a means for identifying the concentration of defects in a material to the environment's oxygen partial pressure and temperature. The defect formation energies calculated from the DFT simulation were used to construct Brouwer diagrams with the aid of a defect analysis package.[76]

For each value of p_{O_2} and T, there is only one Fermi level for which charge neutrality is conserved. Using an initial estimate for the Fermi level, the concentration of electrons and holes is calculated using the experimental bandgap according to Maxwell–Boltzmann statistics:

$$n_e = N_c \exp\left(-\frac{E_g - \mu_e}{kT}\right) \quad (9)$$

$$n_h = N_v \exp\left(\frac{-\mu_e}{kT}\right) \quad (10)$$

where N_c and N_v are the conduction band and valence band density of states. Then, for each defect, the value of ΔE_f^i is calculated using eqn (1), (3) and (6). The concentrations of each defect i is given by:

$$c_i = m_i \exp\left(\frac{-\Delta E_f^i}{kT}\right) \quad (11)$$

where m_i is the multiplicity of the defect. These resulting trial concentrations are then used to calculate the total charge, q_{tot}, from eqn (12)

$$q_{tot} = \sum_i q_i c_i - n_e + n_h \quad (12)$$

and if q_{tot} is positive, the Fermi level is increased and if negative it is reduced. The process is iterated until the self-consistent Fermi level yielding charge neutrality was found for that p_{O_2} and T. The algorithm is then repeated for a range of temperatures and pressures to build Brouwer diagrams.

Results and discussion

Model verification

The calculated lattice parameters were 3.84 Å, 14.38 Å and 3.77 Å, for the a-axis, b-axis and c-axis respectively, which are all

Open Access Article. Published on 23 November 2017. Downloaded on 2/3/2026 3:27:22 PM.
This article is licensed under a Creative Commons Attribution 3.0 Unported Licence.

within 4% of the experimental values of 3.96 Å, 13.86 Å and 3.70 Å reported by Kihlborg *et al.*[77] Fig. 3a and b compare the axis length and bond lengths calculated in the current work with previous computational reports as a percentage of the experimental values. The largest deviation for the axis lengths is observed in the *b*-axis, where the inter-planar distance is dominated by van der Waals interactions. To overcome this, previous studies have fixed the *b*-axis length to the experimental value[47,61,78] resulting in larger bandgaps and lattice parameters which are in closer agreement with experimental values. However, a constrained structure necessarily has internal strains; in turn, these are known to affect the formation energy of the defects considerably, as noted by Huang *et al.*[79] Therefore, all constraints were removed in this study when simulating the defect-free lattice.

The other major differences in axis lengths and bond-lengths that are evident in Fig. 3a and b are caused by differing choices of exchange–correlation functional, on-site Coulomb correction (+*U*) value, and van der Waals forces treatment. This work used the D3 treatment by Grimme,[62] while earlier studies used the D2,[47,80] the optB88-vdW[46,81,82] or in the case of early studies,[53,60,61] no treatment at all. The most common level of theory was GGA + *U* with a *U* parameter of 6.3 eV, however there were studies that used smaller *U* values,[83] no *U* parameter[53] or the HSE06 hybrid functional.[48]

The band gap of the simulated structure of this work was found to be 1.5 eV, which is lower than the experimental values that range from 3 to 3.3 eV.[22,36,38,84] The underestimation of the bandgap is a well-known issue with DFT simulations employing local and semilocal exchange correlation functionals, and the band gap predicted here is close to other values using the same functional, such as the 1.6 eV reported by Huang *et al.*[79] and the 1.7 eV reported by Peelaers *et al.*[85] for the PBE functional. Studies that fixed the *b*-axis reported higher bandgaps of between 1.95 eV [61] and 2.4 eV,[47] in line with results showing that lattice distortion has a significant effect on bandgap.[79] It has been shown that adding a +*U* correction only widens the computed gap by around 0.1 eV or so,[51,52] while the use of the HSE06 hybrid functional produces bandgaps consistent with experimental value,[47,48,85] at the cost of greatly increasing computational complexity.

With Bader analysis,[86] the Bader charges on the oxygen atoms were found to be −0.68*e*, −0.99*e* and −1.10*e*, for the O1, O2 and O3 atoms respectively, with a Bader charge on the Mo of 2.77*e*. These results match within 8% the recent works of Agarwal *et al.*[83] and Akande *et al.*,[48] but have an up to 22% magnitude difference from older studies with no van der Waals treatment such as Coquet & Willock,[60] Sha *et al.*,[53] and Lei & Chen,[52] indicating that van der Waals treatment has a noticeable effect on charge distributions in this material.

Fig. 4 shows the wide discrepancies in oxygen vacancy formation energies in the literature, such as the 2.1 eV difference between the formation energy reported on the $V_{O1}^{\times}$ by Akande *et al.*[48] and that reported in Kim *et al.*[46] These variations are a considerably larger than what is acceptable for meaningful analysis of defect concentration, as there is an exponential dependence of concentration on formation energy. For example, using simple Boltzmann statistics at 300 K, a 1 eV drop in defect formation energy would multiply the predicted defect concentration by a factor of over 10^{17}.

These large defect formation differences are caused by variations of the parameters in eqn (1). The differences in the formation energy of charge neutral vacancies can only be explained by the differing methods of determining the oxygen chemical potential and the variations in computational method already discussed. The differences in the Fermi level at which the cross-over between two charge states occur, are not affected by the oxygen chemical potential, but may be explained by other factors. For example, the use of the 3 × 1 × 3 supercell size without charge correction would make the charged states appear more favourable than they are, as was shown in Fig. 2, making them dominant for larger Fermi levels than are found in this work. An underestimation of the electron potential at the valence band minimum would have the same effect.

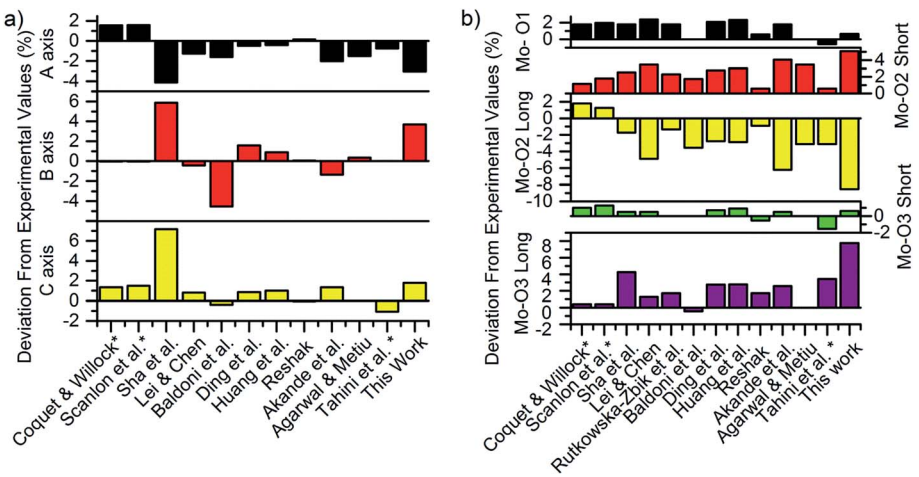

Fig. 3 Deviation of calculated (a) axis lengths and (b) bond lengths compared to experiment for 12 previous studies and this work.[47,48,51–53,60,61,79,82,83,87,88] Star symbols indicate studies that have constrained the *b*-axis to experimental value.

 This journal is © The Royal Society of Chemistry 2017

Open Access Article. Published on 23 November 2017. Downloaded on 2/3/2026 3:27:22 PM.
This article is licensed under a Creative Commons Attribution 3.0 Unported Licence.

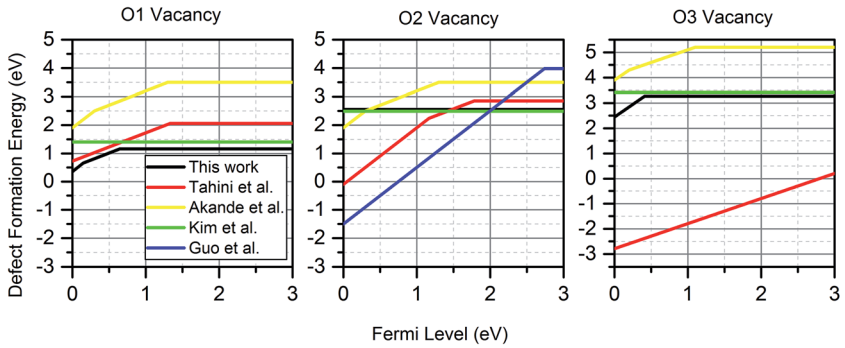

Fig. 4 Comparison of oxygen vacancy formation energies for four previous studies[46–49] and this work. Kim *et al.* only considered charge neutral vacancies. For the V_{O2}, the stable charge neutral state shown is from a larger 4 × 4 × 6 supercell simulation. For studies with multiple charges, only the most dominant charge state at each Fermi level is shown. The values from this work are calculated at a temperature of 300 K and an oxygen partial pressure of 0.2 atm.

Intrinsic defects

There are several types of intrinsic point defects that could occur in MoO_3, consisting of vacancies and interstitials of molybdenum and oxygen atoms. There are three different types of V_{O2}, corresponding to the three sites in α-MoO_3 with different coordination numbers. Three stable sites for were found for Mo_i, shown in Fig. 5a, and three stable sites were found for O_i, shown in Fig. 5b. The Wyckoff positions for these interstitials are presented in Table 3.

Fig. 6 shows the defect formation energy at a temperature of 300 K and p_{O_2} of 0.2 atm for the most favourable charge state of each intrinsic defect as a function of Fermi level. Oxygen vacancies are most easily accommodated on the O1 site, and may take all three charge states but the charge neutral state is predominant for the majority of electron energies in the bandgap. The *i*6 site was found to be the most favourable oxygen interstitial, although it is only slightly more favourable than O_{i5}. Oxygen interstitials are predicted to mostly exhibit the 0 and −2 charge state, with the O_{i5} only exhibiting the charge neutral state. All oxygen interstitials exhibit highly unfavourable formation energies compared to the other defects. Molybdenum vacancies adopt all negative charge states except −4, and −6 while the dominant Mo_{i3} adopts all positive charge states except +4 and +5.

The only other study that considered V_{Mo} was by Akande *et al.*,[48] who predict formation energies in excess of 10 eV higher than the current work. Such large difference cannot be accounted for with the differences in DFT methodology, instead it is likely due to different treatment of the chemical potential. Comparison of formation energy differences between O-rich and O-poor conditions provides further insight: in our methodology, an increase of ΔE in $\mu_{O(MoO_3)}$ yields a necessary decrease of $3\Delta E$ in $\mu_{Mo(MoO_3)}$, as enforced through eqn (5). The same energy shift between O-rich and O-poor is not observed in the work of Akande *et al.*, confirming the use of a different definition of chemical potential.

Fig. 7 shows the Brouwer diagrams of defect concentrations at different values of temperature and p_{O_2}. Fig. 7a shows that at atmospheric pressure, significant numbers of defects do not occur unless the temperature is elevated. The dominant defect by far is the charge neutral oxygen vacancy, with near-negligible amounts of $V_O^{\cdot}$ and $V_{Mo}^{''''''}$ (two orders of magnitude less). These results match the experimental evidence that oxygen vacancies are the dominant defect in MoO_3 films,[89,90] and that the amount of oxygen vacancies is dependent on the pressure[37] and temperature[45] used in sample preparation. The current Brouwer diagrams provide a further clarification of this temperature and pressure dependence.

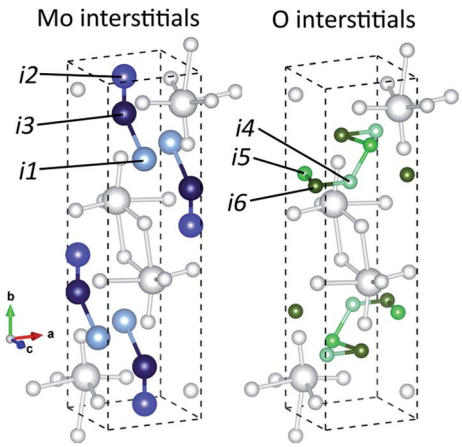

Fig. 5 Interstitial sites found to be stable, with Mo/Si interstitial sites shown on the left in three shades of blue and O interstitial sites shown on the right in three shades of green. Mo and O atoms are shown in white.

Table 3 Wyckoff positions for interstitial sites

Interstitial site	Location	Interstitial atoms stable at site
*i*1	4c (0.5, 0.25, 0.25)	Mo, Si
*i*2	4c (0.5, 0.0425, 0.25)	Mo, Si
*i*3	4c (0.5, 0.15, 0.75)	Mo, Si
*i*4	4c (0.625, 0.3, 0.25)	O
*i*5	4c (0.4, 0.2, 0.25)	O
*i*6	4c (0.5, 0.2, 0.75)	O

Open Access Article. Published on 23 November 2017. Downloaded on 2/3/2026 3:27:22 PM.
This article is licensed under a Creative Commons Attribution 3.0 Unported Licence.

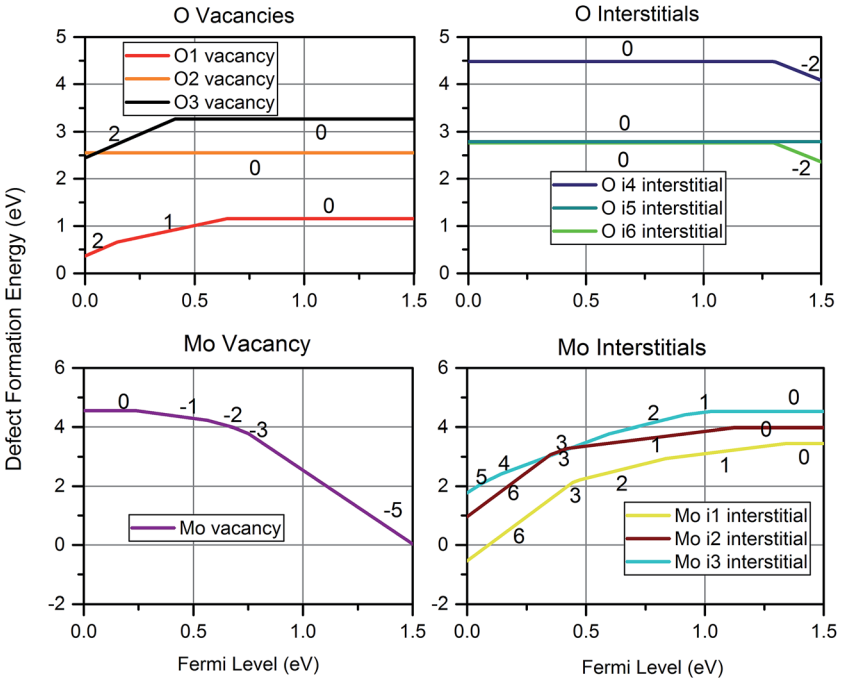

Fig. 6 The formation energy of the dominantly charged defect at each Fermi level for each intrinsic defect at a temperature of 300 K and p_{O_2} of 0.2 atm. The charges of the dominant charge states are labelled.

Fig. 7b shows that if a high temperature anneal is performed under low pressure or low oxygen conditions, a large number of $V_O^{\times}$ will form, along with some Mo_i. The number of oxygen vacancies predicted at the very highest temperatures in Fig. 7b, would make the crystalline structure completely unstable. This matches with the experimental observation that initial thermal

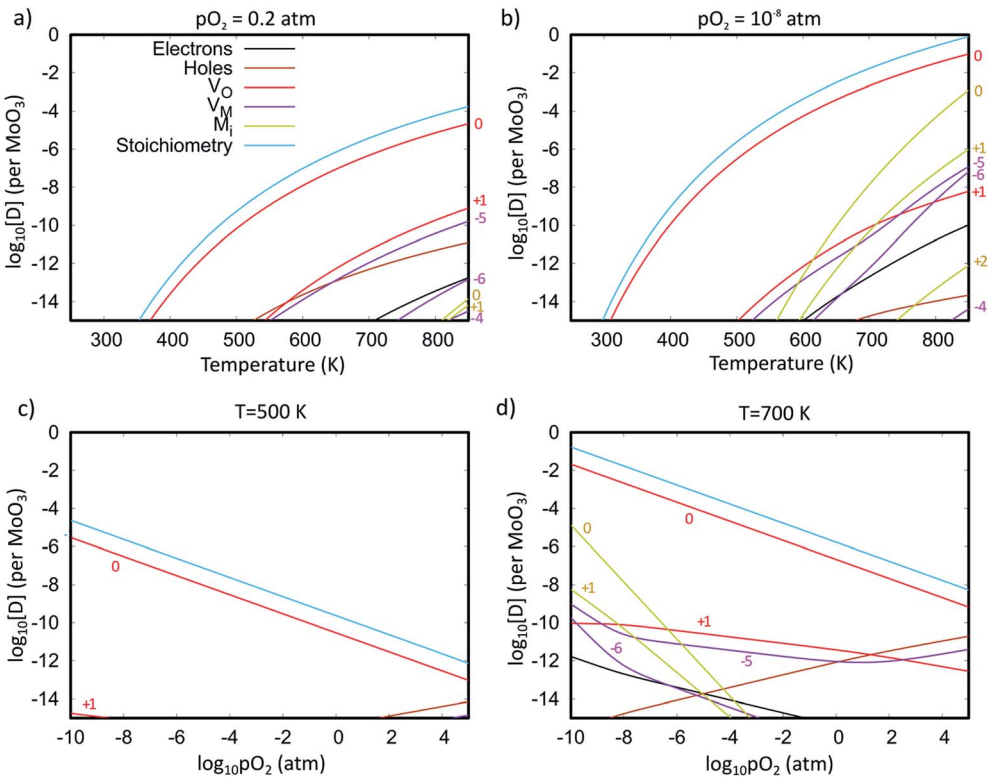

Fig. 7 Brouwer diagrams showing the defect concentrations per formula unit as a function of temperature at constant pressure of (a) 0.2 atm and (b) 10^{-8} atm, and as a function of partial pressure at constant temperatures of (c) 500 K and (d) 700 K. Graphs also include concentrations of electrons and holes and the degree of sub-stoichiometry (x in MoO_{3-x}). The different charge states of each defect type are labelled.

 This journal is © The Royal Society of Chemistry 2017

Open Access Article. Published on 23 November 2017. Downloaded on 2/3/2026 3:27:22 PM.
This article is licensed under a Creative Commons Attribution 3.0 Unported Licence.

evaporations at low pressures in the range of 10^{-9} atm always results in sub-stoichiometric amorphous materials.[21,91,92] These results also are in agreement with the fact that annealing MoO_3 at temperatures of above 550 K in argon atmosphere results in high levels of oxygen vacancies but similar anneals in oxygen atmospheres do not.[36,40] It's worth noting that although the $V_O^{\times}$ is dominant, the charged defects still play a crucial role in determining the Fermi energy that gives yields charge neutrality, which varies within the range of 1.1 eV to 1.9 eV for the pressures and temperatures considered.

Fig. 7c and d show how changing the oxygen partial pressure affects the concentration of defects significantly. The dominance of the $V_O^{\times}$ in the range examined gives us a simple formula for determining the effect of varying oxygen partial pressure: by combining eqn (1), (3) and (11), it can be determined that the concentration of vacancies is inversely proportional to the square root of oxygen partial pressure, eqn (13). This concentration will be the dominant factor affected the stoichiometry of the material.

$$C_{V_O} \propto \frac{1}{\sqrt{p_{O_2}}} \tag{13}$$

The accuracy of the estimated concentration of vacancies is hard to determine as there has been little quantification of defect concentrations in the experimental literature. Sian and Reddy[91] found a degree of sub-stoichiometry x of 0.01 for material annealed in air at 623 K, four orders of magnitude higher than that predicted in Fig. 7. However, the discrepancy may be largely attributed to the reported incomplete crystallisation in the experiment. The Brouwer diagrams also indicate that trace levels of Mo_i defects may be observed at high temperature and low p_{O_2}, but no O_i defects will occur under any of the preparation conditions shown.

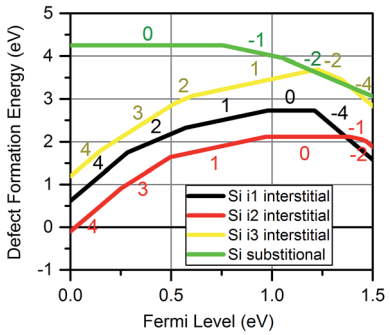

Fig. 8 Defect formation energies for silicon defects inside MoO_3 at the three sites at a temperature of 300 K and p_{O_2} of 0.2 atm. The charges of the dominant charge states are labelled.

Silicon defects

Recent applications of MoO_3, particularly for photovoltaics, have involved MoO_3 junctions with crystalline or amorphous silicon, raising the possibility of silicon penetration into MoO_3 layers. To investigate this, DFT simulations of silicon defects within the MoO_3 crystalline structure were performed. Si_i were

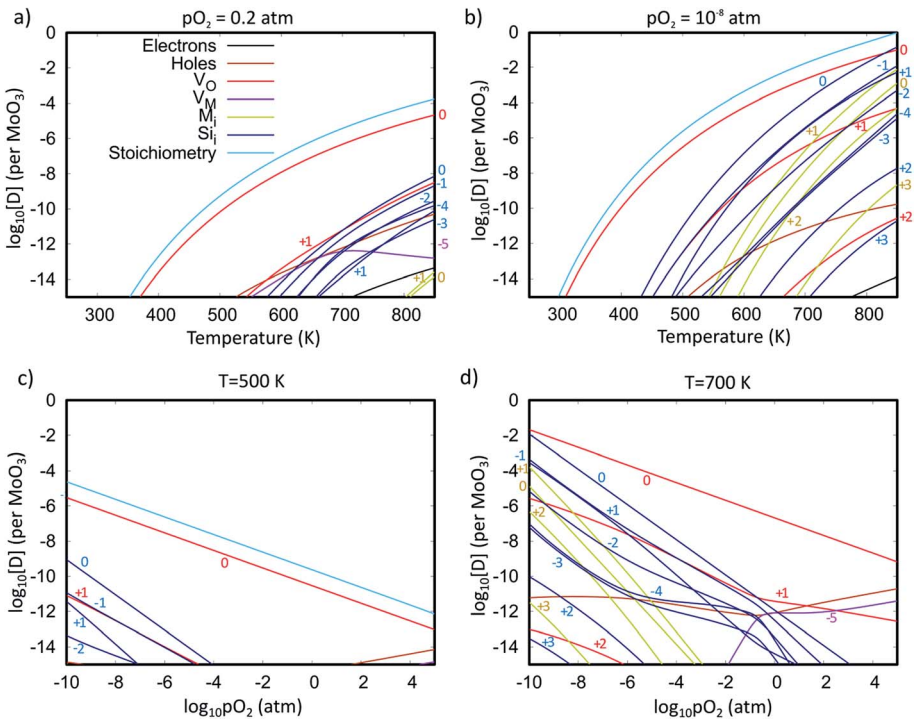

Fig. 9 Brouwer diagrams showing the defect concentrations per formula unit as a function of temperature at constant pressure of (a) 0.2 atm and (b) 10^{-8} atm, and as a function of partial pressure at constant temperatures of (c) 500 K and (d) 700 K. Graphs also include concentrations of electrons and holes and the degree of sub-stoichiometry (x in MoO_{3-x}). The different charge states of each defect type are labelled.

Open Access Article. Published on 23 November 2017. Downloaded on 2/3/2026 3:27:22 PM.
This article is licensed under a Creative Commons Attribution 3.0 Unported Licence.

found to be stable on the same interstitial sites that were found for Mo_i.

Fig. 8 shows the formation energies for silicon defects. This shows that Si_i exhibit amphoteric behaviour within the MoO_3 crystal. For all interstitials, the charge state switches gradually from +4 to +1 as the Fermi energy increases, before shifting to negative charges such as −2 and −4 near the conduction band minimum. The Si_{Mo} was found to be less favourable than any of the Si_i for most of the Fermi level range.

To investigate the accommodation of Si in MoO_3 under different processing conditions, Brouwer diagrams were constructed with silicon defects included, presented in Fig. 9. The Brouwer diagrams show that at high temperature and low p_{O_2}, silicon is highly soluble in MoO_3, and that the preferential presence of Si_i defects prevents the formation of V_{Mo}, which were observed in trace amounts in the intrinsic Brouwer diagrams. The Si_{Mo} defects do not appear under the conditions shown. At all temperatures and pressures, Si_i are more abundant than Mo_i, in fact at all pressures below atmospheric conditions, $Si_i^{\times}$ are the second most prevalent defects after $V_O^{\times}$, although the concentrations are not impactful until low p_{O_2}. Si interstitials are primarily charge neutral, with some +1 and −1 defects also occurring in roughly equal quantities at low p_{O_2}.

These results imply there might be some concern about silicon contamination. Fig. 10 shows the predicted silicon defect concentration as a function of both p_{O_2} and T, indicating that high amounts of contamination may occur under low p_{O_2} and high T conditions. The thermal evaporation process is often performed at pressures below 10^{-9} atm,[21,92] and a crystallisation anneal performed with a temperature of 700 K in an N_2 or Argon ambient with p_{O_2} of 10^{-6} atm is predicted to produce a silicon defect concentration of 1.3 ppm (or 2.5×10^{17} cm^{-3}). These conditions are similar to what is reported in the literature,[20,34] with p_{O_2} estimated on the assumption of 6N purity gasses, indicating that careful consideration of Si interfusion should be taken into account when preparing MoO_{3-x}, either by limiting the temperature, avoiding low pressures, or by reducing the exposure time (provided the kinetics of Si diffusion are slower than that of MoO_3 evaporation).

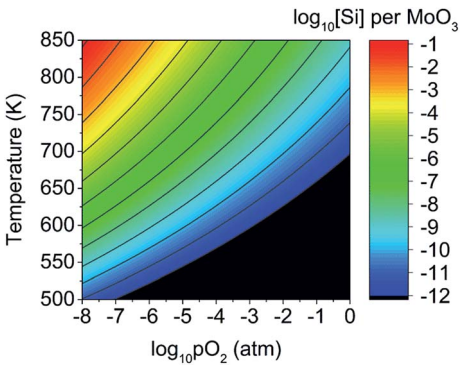

Fig. 10 Predicted concentration of silicon interstitial defects as a function of oxygen partial pressure and temperature. Concentrations below 10^{-12} defects per MoO_3 formula unit are in black.

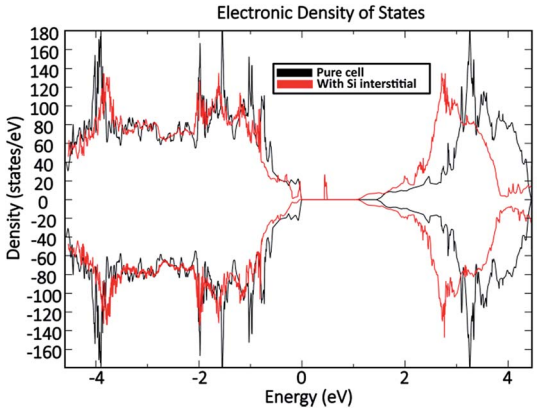

Fig. 11 Computed density of states comparison between an MoO_3 supercell without defects and an MoO_3 supercell containing the dominant silicon interstitial defect.

Fig. 11 shows a comparison of the DOS between a defect-free MoO_3 supercell and one containing the dominant silicon $Si_i^{\times}$ defect. The presence of silicon defects introduces a spin-polarised defect state 0.5 eV above the valence band maximum which consequently reduces the bandgap by 0.3 eV. This result suggests that a high amount of silicon penetration would have a significant impact on the electronic properties of the MoO_3 layer and hence the performance of any MoO_{3-x} based device. Of particular concern, is the increased parasitic absorption in the MoO_{3-x} contact layers which can directly reduce the energy conversion efficiency of silicon photovoltaic devices.

Conclusion

This study has explored the formation of both intrinsic (oxygen vacancies) and extrinsic (silicon interstitials) in crystalline α-MoO_3 under different preparation conditions using *ab initio* DFT. The results of the simulations are compared with previous studies and it was shown that, despite the axis and bond length properties of all previous works agreeing to within 9% of each other, the estimation of the defect formation energies of oxygen vacancies are highly inconsistent with each other. In order to rationalise these differences, a rigorous method for calculating formation energies was established, using an unconventional 2 × 2 × 3 supercell to minimise the electrostatic self-interaction between charged defects. All intrinsic defects were simulated, including the molybdenum and oxygen interstitials which had not been considered previously, and their formation energies were calculated as a function of the Fermi level. The calculated formation energies were then used to produce Brouwer diagrams that showed how the concentration of intrinsic defects varied with changing oxygen partial pressure and temperature. It was predicted (from the Brouwer diagrams) that the charge neutral oxygen vacancy is the most dominant intrinsic defect under the range of conditions considered, but other defects such as molybdenum interstitials could also be present at low p_{O_2} and high temperatures. Furthermore, it was

 This journal is © The Royal Society of Chemistry 2017

Open Access Article. Published on 23 November 2017. Downloaded on 2/3/2026 3:27:22 PM.
This article is licensed under a Creative Commons Attribution 3.0 Unported Licence.

shown that the stoichiometry of the MoO_{3-x} varied as a simple function of p_{O_2} and temperature. These findings can help explain previous experimental results in terms of the effect of preparation conditions on material properties.

The methods used for intrinsic defects were then extended to silicon defects in MoO_3. It was found that silicon is most readily incorporated as an interstitial species, where it introduces a spin-polarised defect state 0.5 eV above the MoO_3 valence band maximum and consequently reduces the bandgap of the metal oxide by 0.3 eV. The silicon defect can reach a concentration of 1.3 ppm at commonly-used processing conditions of 700 K and 10^{-6} atm oxygen partial pressure, and significantly higher concentrations at lower p_{O_2} and/or higher temperatures. This result suggests that silicon contamination of MoO_{3-x} contact layers may represent a serious durability issue for silicon PV cells and modules and may impact device performance due to increased parasitic absorption.

The DFT method outlined in this paper could also be extended to other foreign defects such as hydrogen, which may be of particular interest for silicon solar cells as hydrogen can reduce interface state densities at a crystalline silicon surface. Further modelling could also determine the electronic effects of specific oxygen vacancy defect clusters in this material. The Brouwer diagrams developed through this study could be used to optimise fabrication processes to achieve a target stoichiometry and/or defect concentration. Since the defects have significant effects on material properties, this tuning could have a large effect on the viability of crystalline MoO_{3-x} contacts and hence the development and advancement of efficient and cost-effective MoO_{3-x}-based devices.

Conflicts of interest

There are no conflicts of interest to declare.

Acknowledgements

The authors would like to thanks Dr Tahini for his help and insightful suggestions. This research was undertaken with the assistance of resources and services from the National Computational Infrastructure (NCI), which is supported by the Australian Government, and the Multi-modal Australian ScienceS Imaging and Visualisation Environment (MASSIVE) (http://www.massive.org.au). Access to computational resources was granted through the national merit allocation scheme (NCMAS) and UNSW's "HCP@NCI" trial scheme. Daniel Lambert acknowledges the support of the Australian Government through the award of a Research Training Program (RTP) scholarship. P. A. B. acknowledges the Tyree Foundation and the Australian Nuclear Science and Technology Organisation for financial support.

Notes and references

1 S. H. Lee, Y. H. Kim, R. Deshpande, P. A. Parilla, E. Whitney, D. T. Gillaspie, K. M. Jones, A. Mahan, S. Zhang and A. C. Dillon, *Adv. Mater.*, 2008, **20**, 3627–3632.
2 M. B. Sreedhara, A. L. Santhosha, A. J. Bhattacharyya and C. N. R. Rao, *J. Mater. Chem. A*, 2016, **4**, 9466–9471.
3 F. Li, C. R. Cabrera and Z. Chen, *J. Mater. Chem. A*, 2014, **2**, 19180–19188.
4 Q.-L. Lu, S.-X. Zhao, C.-K. Chen, X. Wang, Y.-F. Deng and C.-W. Nan, *J. Mater. Chem. A*, 2016, **4**, 14560–14566.
5 H. Peng, G. Ma, J. Mu, K. Sun and Z. Lei, *J. Mater. Chem. A*, 2014, **2**, 10384–10388.
6 T. Brezesinski, J. Wang, S. H. Tolbert and B. Dunn, *Nat. Mater.*, 2010, **9**, 146.
7 Z. Ouyang, S. N. Lou, D. Lau, J. Chen, S. Lim, P.-C. Hsiao, D.-W. Wang, R. Amal, Y. H. Ng and A. Lennon, *Adv. Energy Mater.*, 2017, **7**, 1602325.
8 V. Augustyn, P. Simon and B. Dunn, *Energy Environ. Sci.*, 2014, **7**, 1597–1614.
9 K. Galatsis, Y. Li, W. Wlodarski, E. Comini, G. Faglia and G. Sberveglieri, *Sens. Actuators, B*, 2001, **77**, 472–477.
10 M. B. Rahmani, S.-H. Keshmiri, J. Yu, A. Sadek, L. Al-Mashat, A. Moafi, K. Latham, Y. Li, W. Wlodarski and K. Kalantar-Zadeh, *Sens. Actuators, B*, 2010, **145**, 13–19.
11 P. L. Gai-Boyes, *Catal. Rev.: Sci. Eng.*, 1992, **34**, 1–54.
12 J. Haber and E. Lalik, *Catal. Today*, 1997, **33**, 119–137.
13 J. B. Wagner, S. B. Abd Hamid, D. Othman, O. Timpe, S. Knobl, D. Niemeyer, D. S. Su and R. Schlögl, *J. Catal.*, 2004, **225**, 78–85.
14 S. N. Lou, Y. H. Ng, C. Ng, J. Scott and R. Amal, *ChemSusChem*, 2014, **7**, 1934–1941.
15 S. N. Lou, N. Yap, J. Scott, R. Amal and Y. H. Ng, *Sci. Rep.*, 2014, **4**, 7428.
16 A. Guerfi, R. Paynter and L. H. Dao, *J. Electrochem. Soc.*, 1995, **142**, 3457–3464.
17 T. C. Arnoldussen, *J. Electrochem. Soc.*, 1976, **123**, 527–531.
18 J. Yao, B. Loo and A. Fujishima, *Ber. Bunsen-Ges.*, 1990, **94**, 13–17.
19 S. Chen, X. Yu, M. Zhang, J. Cao, Y. Li, L. Ding and G. Shi, *J. Mater. Chem. A*, 2015, **3**, 18380–18383.
20 C. Battaglia, X. Yin, M. Zheng, I. D. Sharp, T. Chen, S. McDonnell, A. Azcatl, C. Carraro, B. Ma and R. Maboudian, *Nano Lett.*, 2014, **14**, 967–971.
21 J. Bullock, A. Cuevas, T. Allen and C. Battaglia, *Appl. Phys. Lett.*, 2014, **105**, 232109.
22 C. Battaglia, S. M. De Nicolas, S. De Wolf, X. Yin, M. Zheng, C. Ballif and A. Javey, *Appl. Phys. Lett.*, 2014, **104**, 113902.
23 X. Fan, M. Zhang, X. Wang, F. Yang and X. Meng, *J. Mater. Chem. A*, 2013, **1**, 8694–8709.
24 J. Meyer, S. Hamwi, M. Kröger, W. Kowalsky, T. Riedl and A. Kahn, *Adv. Mater.*, 2012, **24**, 5408–5427.
25 C. Girotto, E. Voroshazi, D. Cheyns, P. Heremans and B. P. Rand, *ACS Appl. Mater. Interfaces*, 2011, **3**, 3244–3247.
26 S. Ranjbar, G. Brammertz, B. Vermang, A. Hadipour, S. Cong, K. Suganuma, T. Schnabel, M. Meuris, A. da Cunha and J. Poortmans, *Phys. Status Solidi A*, 2017, **214**, 1600534.
27 K. Zilberberg and T. Riedl, *J. Mater. Chem. A*, 2016, **4**, 14481–14508.
28 M. Acik and S. B. Darling, *J. Mater. Chem. A*, 2016, **4**, 6185–6235.

Open Access Article. Published on 23 November 2017. Downloaded on 2/3/2026 3:27:22 PM.
This article is licensed under a Creative Commons Attribution 3.0 Unported Licence.

29 C.-W. Chen, S.-Y. Hsiao, C.-Y. Chen, H.-W. Kang, Z.-Y. Huang and H.-W. Lin, *J. Mater. Chem. A*, 2015, **3**, 9152–9159.
30 Y. Zhao, A. M. Nardes and K. Zhu, *Appl. Phys. Lett.*, 2014, **104**, 213906.
31 J. Geissbühler, J. Werner, S. M. de Nicolas, L. Barraud, A. Hessler-Wyser, M. Despeisse, S. Nicolay, A. Tomasi, B. Niesen and S. De Wolf, *Appl. Phys. Lett.*, 2015, **107**, 081601.
32 M. Taguchi, A. Yano, S. Tohoda, K. Matsuyama, Y. Nakamura, T. Nishiwaki, K. Fujita and E. Maruyama, *IEEE J. Photovolt.*, 2014, **4**, 96–99.
33 A. L. F. Cauduro, R. dos Reis, G. Chen, A. K. Schmid, C. Méthivier, H.-G. Rubahn, L. Bossard-Giannesini, H. Cruguel, N. Witkowski and M. Madsen, *ACS Appl. Mater. Interfaces*, 2017, **9**, 7717–7724.
34 M. Sook Oh, B. Seob Yang, J. Ho Lee, S. Ha Oh, U. Soo Lee, Y. Jang Kim, H. Joon Kim and M. Soo Huh, *J. Vac. Sci. Technol., A*, 2012, **30**, 031501.
35 M. T. Greiner, L. Chai, M. G. Helander, W. M. Tang and Z. H. Lu, *Adv. Funct. Mater.*, 2012, **22**, 4557–4568.
36 A. Bouzidi, N. Benramdane, H. Tabet-Derraz, C. Mathieu, B. Khelifa and R. Desfeux, *Mater. Sci. Eng., B*, 2003, **97**, 5–8.
37 A. L. F. Cauduro, Z. E. Fabrim, M. Ahmadpour, P. F. Fichtner, S. Hassing, H.-G. Rubahn and M. Madsen, *Appl. Phys. Lett.*, 2015, **106**, 202101.
38 K. Kanai, K. Koizumi, S. Ouchi, Y. Tsukamoto, K. Sakanoue, Y. Ouchi and K. Seki, *Org. Electron.*, 2010, **11**, 188–194.
39 K. Eda, *J. Solid State Chem.*, 1991, **95**, 64–73.
40 S. Deb and J. Chopoorian, *J. Appl. Phys.*, 1966, **37**, 4818–4825.
41 Y. Li, D. Wang, Q. An, B. Ren, Y. Rong and Y. Yao, *J. Mater. Chem. A*, 2016, **4**, 5402–5405.
42 S. Balendhran, J. Deng, J. Z. Ou, S. Walia, J. Scott, J. Tang, K. L. Wang, M. R. Field, S. Russo and S. Zhuiykov, *Adv. Mater.*, 2013, **25**, 109–114.
43 S. Balendhran, S. Walia, H. Nili, J. Z. Ou, S. Zhuiykov, R. B. Kaner, S. Sriram, M. Bhaskaran and K. Kalantar-zadeh, *Adv. Funct. Mater.*, 2013, **23**, 3952–3970.
44 C. Julien, A. Khelfa, O. Hussain and G. Nazri, *J. Cryst. Growth*, 1995, **156**, 235–244.
45 M. Dieterle, G. Weinberg and G. Mestl, *Phys. Chem. Chem. Phys.*, 2002, **4**, 812–821.
46 H.-S. Kim, J. B. Cook, H. Lin, J. S. Ko, S. H. Tolbert, V. Ozolins and B. Dunn, *Nat. Mater.*, 2016, **16**, 454–460.
47 H. A. Tahini, X. Tan, S. N. Lou, J. Scott, R. Amal, Y. H. Ng and S. C. Smith, *ACS Appl. Mater. Interfaces*, 2016, **8**, 10911–10917.
48 S. O. Akande, A. Chroneos, M. Vasilopoulou, S. Kennou and U. Schwingenschlögl, *J. Mater. Chem. C*, 2016, 9526–9521.
49 Y. Guo and J. Robertson, *Appl. Phys. Lett.*, 2014, **105**, 222110.
50 M. Anwar and C. Hogarth, *J. Mater. Sci.*, 1990, **25**, 4918–4928.
51 M. Baldoni, L. Craco, G. Seifert and S. Leoni, *J. Mater. Chem. A*, 2013, **1**, 1778–1784.
52 Y.-H. Lei and Z.-X. Chen, *J. Phys. Chem. C*, 2012, **116**, 25757–25764.
53 X. Sha, L. Chen, A. C. Cooper, G. P. Pez and H. Cheng, *J. Phys. Chem. C*, 2009, **113**, 11399–11407.
54 J. Handzlik and J. Ogonowski, *J. Phys. Chem. C*, 2012, **116**, 5571–5584.
55 R. Radhakrishnan, C. Reed, S. Oyama, M. Seman, J. Kondo, K. Domen, Y. Ohminami and K. Asakura, *J. Phys. Chem. B*, 2001, **105**, 8519–8530.
56 S. Chempath, Y. Zhang and A. T. Bell, *J. Phys. Chem. C*, 2007, **111**, 1291–1298.
57 G. Kresse and J. Furthmüller, *Phys. Rev. B: Condens. Matter Mater. Phys.*, 1996, **54**, 11169.
58 J. P. Perdew, K. Burke and M. Ernzerhof, *Phys. Rev. Lett.*, 1996, **77**, 3865.
59 S. Dudarev, G. Botton, S. Savrasov, C. Humphreys and A. Sutton, *Phys. Rev. B: Condens. Matter Mater. Phys.*, 1998, **57**, 1505.
60 R. Coquet and D. J. Willock, *Phys. Chem. Chem. Phys.*, 2005, **7**, 3819–3828.
61 D. O. Scanlon, G. W. Watson, D. Payne, G. Atkinson, R. Egdell and D. Law, *J. Phys. Chem. C*, 2010, **114**, 4636–4645.
62 S. Grimme, J. Antony, S. Ehrlich and H. Krieg, *J. Chem. Phys.*, 2010, **132**, 154104.
63 N. D. M. Hine, K. Frensch, W. M. C. Foulkes and M. W. Finnis, *Phys. Rev. B: Condens. Matter Mater. Phys.*, 2009, **79**, 024112.
64 M. Finnis, A. Lozovoi and A. Alavi, *Annu. Rev. Mater. Res.*, 2005, **35**, 167–207.
65 P. J. Linstrom and W. Mallard, in *NIST Chemistry webbook; NIST standard reference database No. 69*, 2001.
66 S. T. Murphy and N. D. Hine, *Phys. Rev. B: Condens. Matter Mater. Phys.*, 2013, **87**, 094111.
67 R. Rurali and X. Cartoixà, *Nano Lett.*, 2009, **9**, 975–979.
68 F. Kröger and H. Vink, *Solid State Phys.*, 1956, **3**, 307–435.
69 S. Lany and A. Zunger, *Phys. Rev. B: Condens. Matter Mater. Phys.*, 2008, **78**, 235104.
70 S. Lany and A. Zunger, *Modell. Simul. Mater. Sci. Eng.*, 2009, **17**, 084002.
71 C. Varvenne, F. Bruneval, M.-C. Marinica and E. Clouet, *Phys. Rev. B: Condens. Matter Mater. Phys.*, 2013, **88**, 134102.
72 P. A. Burr and M. W. D. Cooper, *Phys. Rev. B*, 2017, **96**, 094107.
73 L. Lajaunie, F. Boucher, R. Dessapt and P. Moreau, *Phys. Rev. B: Condens. Matter Mater. Phys.*, 2013, **88**, 115141.
74 J. Du, V. Anye, E. Vodah, T. Tong, M. Zebaze Kana and W. Soboyejo, *J. Appl. Phys.*, 2014, **115**, 233703.
75 R. Hill, *Proc. Phys. Soc., London, Sect. A*, 1952, **65**, 349.
76 S. T. Murphy and N. D. Hine, *Chem. Mater.*, 2014, **26**, 1629–1638.
77 L. Kihlborg, *Ark. Kemi*, 1963, **21**, 357.
78 R. Coquet and D. J. Willock, *Phys. Chem. Chem. Phys.*, 2005, **7**, 3819–3828.
79 P.-R. Huang, Y. He, C. Cao and Z.-H. Lu, *Sci. Rep.*, 2014, **4**, 7131.
80 S. Grimme, *J. Comput. Chem.*, 2006, **27**, 1787–1799.
81 J. Klimeš, D. R. Bowler and A. Michaelides, *Phys. Rev. B: Condens. Matter Mater. Phys.*, 2011, **83**, 195131.
82 H. Ding, K. G. Ray, V. Ozolins and M. Asta, *Phys. Rev. B: Condens. Matter Mater. Phys.*, 2012, **85**, 012104.
83 V. Agarwal and H. Metiu, *J. Phys. Chem. C*, 2016, **120**, 19252–19264.

 This journal is © The Royal Society of Chemistry 2017

84 M. Kroger, S. Hamwi, J. Meyer, T. Riedl, W. Kowalsky and A. Kahn, *Appl. Phys. Lett.*, 2009, **95**, 123301.
85 H. Peelaers and C. G. Van de Walle, *J. Phys.: Condens. Matter*, 2014, **26**, 305502.
86 E. Sanville, S. D. Kenny, R. Smith and G. Henkelman, *J. Comput. Chem.*, 2007, **28**, 899–908.
87 D. Rutkowska-Zbik, R. Grybos and R. Tokarz-Sobieraj, *Struct. Chem.*, 2012, **23**, 1417–1424.
88 A. H. Reshak, *RSC Adv.*, 2015, **5**, 22044–22052.
89 S. K. Deb, *Proc. R. Soc. London, Ser. A*, 1968, **304**, 211–231.
90 M. T. Greiner and Z.-H. Lu, *NPG Asia Mater.*, 2013, **5**, e55.
91 T. S. Sian and G. Reddy, *Sol. Energy Mater. Sol. Cells*, 2004, **82**, 375–386.
92 S. Chuang, C. Battaglia, A. Azcatl, S. McDonnell, J. S. Kang, X. Yin, M. Tosun, R. Kapadia, H. Fang and R. M. Wallace, *Nano Lett.*, 2014, **14**, 1337–1342.

Open Access Article. Published on 23 November 2017. Downloaded on 2/3/2026 3:27:22 PM.
This article is licensed under a Creative Commons Attribution 3.0 Unported Licence.